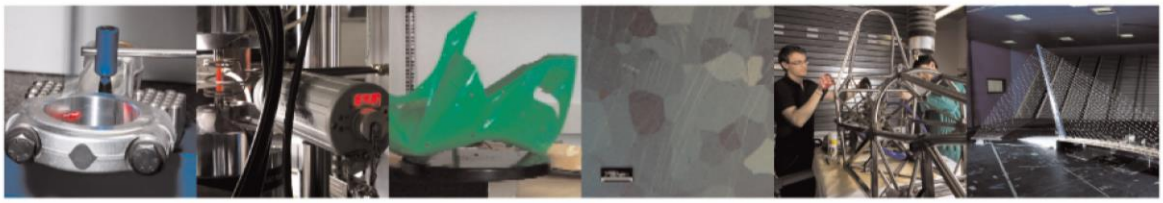

The influence of laser processing parameters on the densification and surface morphology of pure Fe and Fe-35Mn scaffolds produced by selective laser melting

Carluccio, D.; Demir, A. G.; Caprio, L.; Previtali, B.; Bermingham, M. J.; Dargusch, M. S.

This is a post-peer-review, pre-copyedit version of an article published in JOURNAL OF MANUFACTURING PROCESSES. The final authenticated version is available online at: http://dx.doi.org/10.1016/j.jmapro.2019.03.018

The Influence of Laser Processing Parameters on the Densification and Surface Morphology of Pure Fe and Fe-35Mn Scaffolds Produced by Selective Laser Melting

D. Carluccio[ac1], A.G. Demir[b], L. Caprio[b], B. Previtali[b], M.J. Bermingham[ac], M.S. Dargusch[ac]

[a] School of Mechanical and Mining Engineering and Queensland Centre for Advanced Materials Processing and Manufacturing (AMPAM), The University of Queensland, Australia

[b] Department of Mechanical Engineering, Politecnico di Milano, Via La Masa 1, 20156 Milan, Italy

[c] Australian Research Council Research Hub for Advanced Manufacturing of Medical Devices

Abstract

Highly customisable implants with optimised lattice structures can be achieved using selective laser melting (SLM) paving the way for tailored biodegradable Fe-based implants. For the first time, a systematic analysis is presented in terms of laser processing conditions required for scaffolds of pure Fe and a binary Fe-35Mn alloy. The processability of the two materials were compared in terms of densification behaviour, surface roughness and geometrical error. Both materials were successfully processed into high quality scaffolds with excellent strut morphology and low processing porosity. The differences in the laser processing conditions between the pure metal and the binary alloy were discussed. The lower melting temperature of the Fe-35Mn alloy required lower energy density for reaching the fully dense condition. Surface roughness and geometrical errors were found to be similar for the two materials. The microstructure of pure Fe was characterized by equiaxed α-ferrite grains, whereas the Fe-35Mn had a microstructure consisting of columnar γ grains, with each γ-grain comprising of a network of individual cells.

Keywords

Selective Laser Melting; Biodegradable Iron; Bone Scaffolds; Microstructure

1. Introduction

Autologous bone grafting has long been the "gold standard" for the treatment of critical bone defects (CBD) [1-3]. However, major complications like donor site morbidity can lead to chronic pain at the donor site [4, 5]. Furthermore, autologous bone grafting requires multiple surgeries, increasing the risk of surgical complications and resulting in a higher cost when compared to other options [6]. Alternative treatment methods such as bone scaffolds have garnered significant interest recently [7-10]. Bone scaffolds fill the CBD providing a 3-D structure to allow for cell seeding, attachment and subsequent proliferation leading to bone regeneration [11]. An ideal bone scaffold should:

[1] Corresponding author: d.carluccio@uq.edu.au

- be biocompatible and ideally promote bone growth [12];
- have adequate mechanical properties to match the host bone and allow for proper load transfer during healing [13];
- have interconnected pores with adequate pore size to allow for diffusion of oxygen and nutrients [13];
- be fully biodegradable leaving behind no residue in the implantation site [14].

Significant research has been performed on polymer and ceramic scaffolds as they have excellent biocompatibility, can be biodegradable and promote bone growth [3, 7, 10]. For load bearing applications however, these material classes generally cannot maintain the structural integrity required during bone healing [15]. Permanent metallic scaffolds manufactured from tantalum [16, 17], CoCr [18, 19] and titanium alloys [20, 21] have much better mechanical properties and have been tested *in vivo* with some success. Problems associated with these scaffolds are their permanent nature and large mismatch in stiffness between the implant and bone, leading to complications such as peri-implant cell death [22] and bone resorption [23].

Biodegradable metallic (BDM) implants have shown great potential in overcoming drawbacks of other bone scaffold materials. BDMs corrode gradually in the body, and should induce an adequate host response to implantation and degradation [24]. The bulk corrosion product of BDMs should be easy to metabolise in large doses and secondary corrosion products should be non-toxic in the quantities released [25]. Mg, Fe and Zn have been the most extensively researched biodegradable metals [24, 25].

Mg is difficult to manufacture due to its poor formability [26], and its high corrosion rate significantly affects the mechanical integrity of the scaffold during healing [24, 27, 28]. Zn, on the other hand, has a very suitable corrosion rate for BDM applications [29]. However, for load-bearing scaffolds, most biocompatible Zn based alloys do not have sufficient mechanical properties [30]. Additionally, there are concerns regarding the toxicity of Zn in large doses, especially in orthopaedic settings [31]. Compared to the other BDMs, Fe has excellent mechanical properties, and slower degradation rates, often too slow [32]. The addition of Mn to the Fe results in a less noble solid solution that increases the corrosion rate of the alloy [33]. Furthermore, additions of Mn improve the MRI compatibility, formability and mechanical properties [34].

In the past the majority of research on pure Fe and Fe-based alloys as a BDM has focused on cardiovascular applications [35-37], with a recent shift of interest to bone scaffold applications [38, 39]. To the author's knowledge no one has produced Fe-Mn scaffolds via selective laser melting (SLM) for bone scaffold applications. SLM is a highly promising additive manufacturing technology for bone scaffold manufacturing that can produce highly customisable implants with optimised lattice structures, interconnected pores and controllable pore sizes which has been shown to promote bone growth into the implant [20]. Titanium [20, 40], tantalum [41, 42] and stainless steel [43, 44] bone scaffolds have already been successfully manufactured using SLM.

Relatively little work has been done on the selective laser melting of biodegradable bone scaffolds. The properties of biodegradable metals can render them difficult for processing. Magnesium is challenging to process due to its high volatility and flammability, especially in powder form. Despite this, magnesium scaffolds have been

successfully manufactured using SLM [45-48]. However, porous implants have a larger surface area than bulk counterparts resulting in faster corrosion of the scaffold [46]. Of these only Liu et al. investigated the effect of laser processing parameters on the properties of porous Mg-based alloys [48]. It was found that increasing the energy density increased the mechanical properties as doing so decreased the porosity of the samples. At higher energy densities the melt pool stability increased resulting in denser components. The surface morphology however, was found optimised at an energy density of around 875-1000 J/mm^3 since values below this threshold result in incomplete melting of the powder and balling effect. At energy densities past this threshold melt pool instabilities and recoil pressure due to evaporation occurred reducing the surface quality. Jauer et al studied the gas flow to stabilize the processing conditions under severe vapour formation [49]. Under controlled atmosphere bulk and lattice specimens could be manufactured [46, 50].

While less flammable than Mg, Zn also has a relatively small difference between melting point and vaporization point [51, 52] reducing its SLM processability. Demir et al. achieved a processed density of over 99 % using a bespoke SLM machine but had problems with the evaporation of Zn [53]. Similarly, Wen et al. successfully manufactured high density bulk Zn [54, 55] and were the first, and so far only, to produce porous Zn scaffolds [56]. Wen et al. focused on post processing and the effect of shielding gas flow, as this aspect was previously found to significantly increase the density of laser deposited Zn [52]. While Zn scaffolds were successfully produced, the recoil force due to evaporation still proved to be problematic as it increased surface roughness and processing porosity [54].

Research on the selective laser melting of pure Fe and Fe-based alloys has mostly focused on maraging steels, tools steels and other steels used in industry [57]. There has been a relatively limited amount of work on the powder bed fusion of Fe for biomedical applications. SLM of bulk pure Fe was readily achieved and found to have mechanical properties similar to the as cast and wrought equivalent Fe [58, 59]. To improve the corrosion rate, Niendorf et al. processed an Fe-Mn-Ag based alloy via SLM and found that the silver minimally affects the mechanical properties of the part but increases the corrosion rate by about 35% when compared to pure TWIP steel [60]. There is an inherent difference between the processing of bulk and fine geometries [61], as such different processing parameter studies must be performed for bulk samples and scaffolds of the same material. Selective laser melted Fe scaffolds for biomedical applications have been successfully manufactured and despite the increased corrosion rate due to the porous nature of the lattice scaffold, sufficient mechanical properties were retained after 28 days of immersion [39]. This study was the first to produce biodegradable Fe scaffolds, however processing characteristics were not given. Evidently, further studies are required to develop the processes for new alloys designed for biodegradable implant productions.

Through the correct implementation of strategies including process parameter selection, SLM can achieve complex geometries not achievable by traditional manufacturing methods. A greater understanding of the material processability is required particularly on the effect of process parameters on the geometrical error, roughness, porosity and microstructure. Hence, the aim of this paper is to further study the optimal laser processing conditions of biodegradable pure Fe and Fe-35Mn alloy lattice scaffolds manufactured using SLM.

2. Materials and Methods

2.1 Materials

Gas atomized powders were used throughout the study. Samples were manufactured using spherical Fe powder with 99.8 % purity and a particle size distribution of ≤ 45 µm (TLS Technik, Bitterfeld, Germany). Spherical Fe-35Mn alloy powder was characterized by a particle size distribution between ≤ 44 µm (CEAIT, San Sebastian, Spain). The powder morphologies and compositions are shown in Figure 1 and Table 1 respectively. The baseplate material was a mild steel.

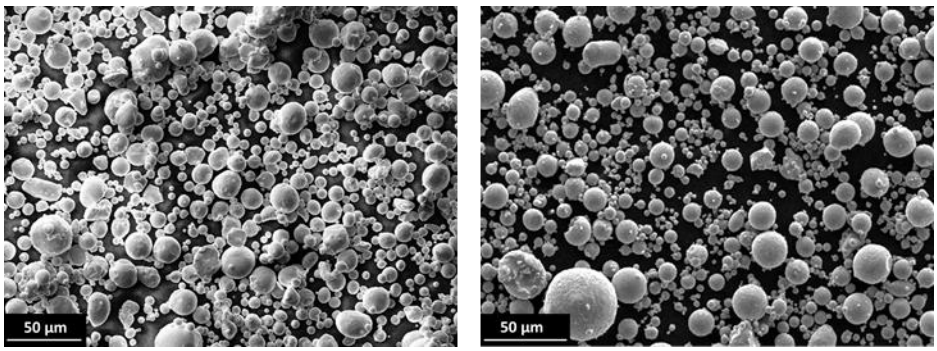

Figure 1 Powder morphology of Pure Fe powder (left) and Fe-35Mn powder (right)

Table 1 Powder chemical composition (all values are expressed in wt%).

Material	Fe	C	Mn	Si	S	P	Ni	Cr	Mo
Pure Fe	Bal.	0.01	0.01	< 0.02	0.01	0.01	<0.01	0.03	< 0.01
Fe-35Mn	Bal.	0.02	32.5	0.03	0.01	0.01	0.01	0.01	0.02

2.2 Selective Laser Melting system

Samples were produced using an industrial selective laser melting system (Renishaw AM250, Stone, UK) using a 200 W single mode fibre laser with an estimated beam size of 75 µm. The laser is power modulated by fast electronic switching to generate pulsed wave (PW) emission. The machine was fitted with a reduced build volume (RBV) kit, providing a smaller build volume (78x78x55 mm^3) for testing small batches of powder. The machine was operated under Ar atmosphere. Prior to the builds, the chamber was evacuated down to a pressure of -950 mbar and then flooded with Ar to produce a 15 mbar overpressure. The oxygen content was maintained below 1000 ppm during the process. Build preparation and process parameter assignment were done using Magics 19 (Materialise, Leuven, Belgium).

2.3 Experimental Plan

The SLM system provides control over several laser and scan strategy parameters, which were evaluated differently for bulk and thin geometries. During the PW emission of the laser, the beam is manipulated between

different exposure positions with a point distance (d_p), where a determined pulse duration (t_{on}) is exposed with the chosen laser power (P). By the end of each scan vector the beam jumps to the consecutive vector placed at a fixed hatch distance (d_h). The focal position of the beam (f) was fixed at the powder bed plane for all the tested conditions in order to maintain a well-focused beam required for the small dimensions of the struts.

Table 2 Process parameters used for lattice specimens.

Fixed parameters	
Focal position, *f* (mm)	0
Layer thickness, *z* (μm)	50
Varied parameters	Range
Peak power, *P* (W)	100-150
Pulse duration, t_{on} (μs)	40-60
Point and hatch distance d_p=d_h (μm)	40-50

The energy density for a power modulated laser running in pulsed wave regime can be calculated using the following expression.

$$E = \frac{P \cdot t_{on}}{d_p \cdot d_h \cdot z} \quad (1)$$

The energy density was varied between 32 and 113 J/mm3 for producing the specimens on both the materials. This was achieved by employing laser power levels between 100 and 150 W, pulse durations between 40 and 60 μs and hatch and point distances varied together between 40 and 60 μm. For thin struts it has been shown that the use of same point and hatch distances is favourable for maintaining dimensional accuracy [61]. Rather, the control over melt pool size, ergo, the energy density is crucial. The layer thickness has an important impact on energy density, and hence the porosity formation, as well as part resolution and productivity. The use of lower layer thickness values could be considered for improved process resolution. Beyond the mechanical capability of the z-axis of the system, the smallest layer thickness is related to the powder size. After laser melting, assuming a complete melting, the density of the solid metal will be higher than the powder apparent density. With constant mass and area, the resultant zone will be lower in height compared to the initial situation. At the consecutive layer, the deposited powder will have to fill in a total height comprised of the axis movement (layer thickness) and the void generated by the density change [62, 63]. Considering a powder bed tap density of approximately 50%, the real layer effective layer thickness settles to the twice of the commanded one. In order to accommodate the largest grains within powder size distribution of the present materials the limit value is approximately 25 μm. Concerning the productivity, the reduction in the layer thickness has an impact on the recoating duration, which would depend highly on the number of layers. As a compromise between all different factors. 50 μm was chosen, which would result in 100 layers to manufacture the lattice scaffold and 12 layers for the size of one strut. No border, upskin or downskin passes were employed.

Lattice scaffolds were designed based on Schwarz Primitive Surface p-unit cells as shown in

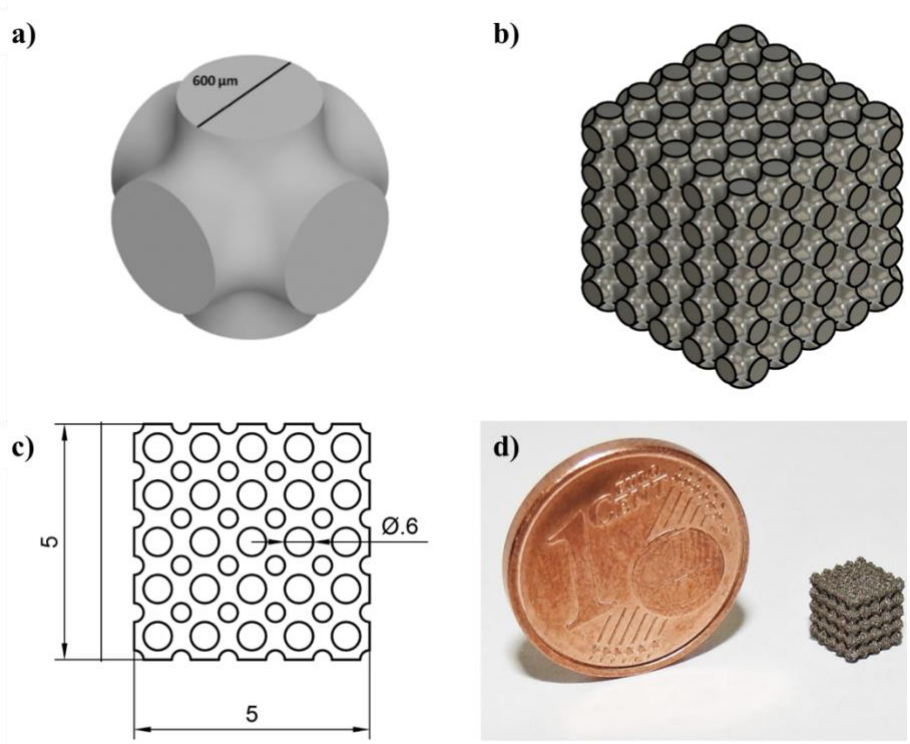

Figure 2. P-unit cells are very suitable for bone scaffolds as they have been shown to have excellent fluid permeability, stress distribution and a high strength-to-weight ratio [64, 65]. Scaffolds were designed to incorporate 5 unit cells in all three directions and have a maximum strut size of 600 µm and an overall porosity of 42 %. Lattice scaffolds were used for density characterization, microhardness and microstructural analysis. Surface roughness and geometrical error measurements required longer struts. Accordingly, strut equivalent rods with the same process conditions were produced. This was achieved by producing the vertical rods with the same diameter of the struts in the lattice scaffolds (600 µm) and the same parameter set as the lattice scaffolds. The rods were positioned next to their equivalent lattice scaffold to maintain a similar heat exchange with the powder bed.

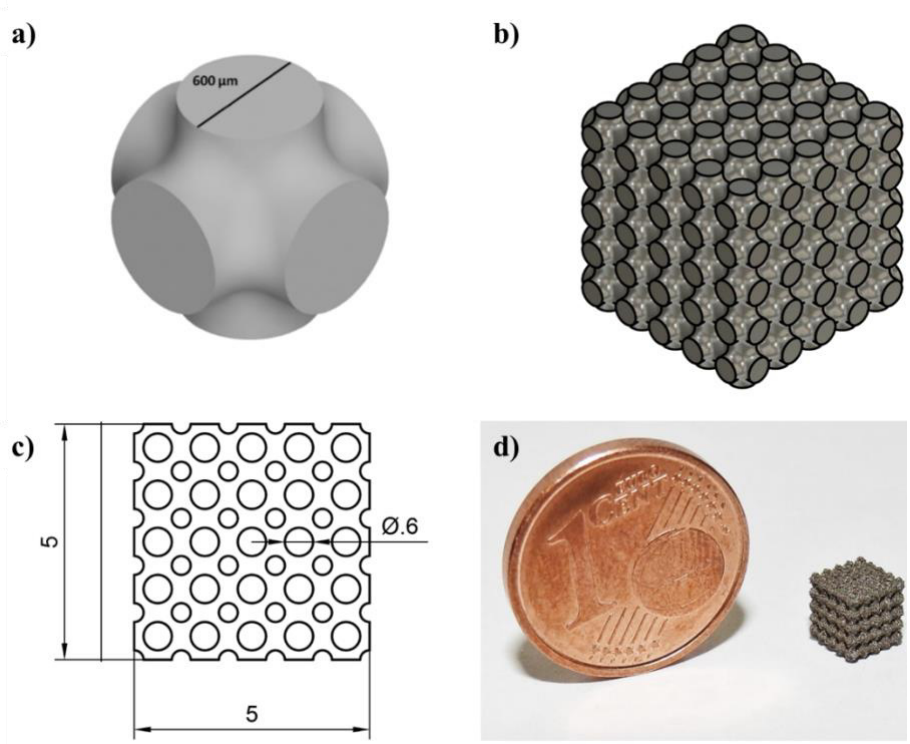

Figure 2 a) The 1x1x1 mm3 Schwarz Primitive Surface unit cell. b) The designed lattice scaffold, and c) its main dimensions. d) Macro image of the produced lattice scaffolds.

2.4 Characterization

The surfaces of the as-built samples were observed using scanning electron microscopy (SEM) (EVO-50, Carl Zeiss, Germany). Characterization of the surface quality was performed on the as-built surfaces using focus variation microscopy (InfiniteFocus, Alicona Imaging GmbH, Austria). The surface quality was measured on equivalent cylindrical rods along the build direction employing the linear average surface roughness (R_a), root mean squared roughness (R_q), and average distance between the highest peak and lowest valley (R_z). Images were acquired over the whole surface using a 5× objective lens. The axial and lateral resolutions were 7 and 3.9 µm respectively. Roughness profile was extracted from the acquired images using a short-pass Gaussian cut off length at 800 µm. Strut diameter was measured on the equivalent as-built cylindrical parts using a universal horizontal measurement system (DMS 680, Microrep Joint Instruments, Italy). The radial deviation was calculated using:

$$e_r = D_m - D_n \tag{2}$$

Where D_m is the measured diameter and D_n is the nominal diameter.

The processed density of the scaffolds was measured using:

$$\rho(\%) = \left(1 - \frac{M_{air}}{M_{ideal}}\right) \cdot 100 \tag{3}$$

Where ρ is processed density of the scaffold and represents a measure of the dimensional errors after SLM, M_{air} is the mass of scaffold in air and M_{ideal} is the theoretical mass of a solid cube of the same material with same dimensions.

The processing porosity of the struts were measured on metallographic sections. All samples were cut perpendicular to the scan direction then mounted, ground and mechanically polished following standard metallographic procedures. Optical microscopy (Polyvar Met, Reichert, USA) followed by image processing was used to determine the processing porosity given by:

$$\Phi\ (\%) = \left(1 - \frac{A_{Pore,tot}}{A_{tot}}\right) \cdot 100 \qquad (4)$$

Where $A_{Pore,tot}$ is the total pore area and A_{tot} is the total area. It is important to note that the processing porosity is a measure of the formational defects that occur during processing and thus excludes the area of the designed pores of the scaffold.

Microhardness testing (Duramin, Struers, Denmark) was performed on bulk pure Fe and Fe35-Mn processed with an energy density of 67 J/mm3 using a 100 gf with a 12 second hold time. For microstructural characterization pure Fe scaffolds produced with an energy density of 72 J/mm3 and Fe-35Mn scaffolds produced with an energy density of 62J/mm3 were cut perpendicular and parallel to the build direction, mounted, mechanically ground and polished followed by etching with Nital to reveal the microstructure. Optical microscopy and SEM (TM3030, Hitachi, Japan) were used to observe the microstructure. Grain size analysis was done using the linear intercept method based on ASTM E112-13 [66].

3. Results and Discussion

3.1 Surface Morphology

When selective laser melting bulk samples the processed density should be as high as possible as porosities can reduce the mechanical properties. For load-bearing bone scaffolds the ideal scaffold should resemble the CAD model as closely as possible. This is determined not only by the processing porosity of the struts, but by the strut and pore morphology and processed density. Based on this criteria, the highest quality scaffolds were achieved at an energy density of 72 J/mm3 for pure Fe and 62 J/mm3 for Fe-35Mn. Figure 3 shows that overall the higher T_m of the pure Fe made it harder to process into scaffolds than the Fe-35Mn. Furthermore, the processability of the pure Fe was further hindered by the powder particle size. From Figure 1 it can be seen that the Fe powder had a larger quantity of smaller particles, this causes partial sintering of the powder next to the melt pool resulting in the designed pores being filled with partially melted powder causing significant deviations from the designed geometry. On the other hand, at the optimised energy density, the Fe-35Mn had more clearly defined struts and pores that most closely resembled the original CAD model. This is also confirmed by the geometrical error

measurements shown in Figure 4. Another aspect underlined by Figure 4 is that in general, an increase in the energy density increases the dimensional error of the struts. This is because as energy density increases, the melt pool becomes larger, resulting in larger struts and as a consequence smaller designed porosities as seen in Figure 3.

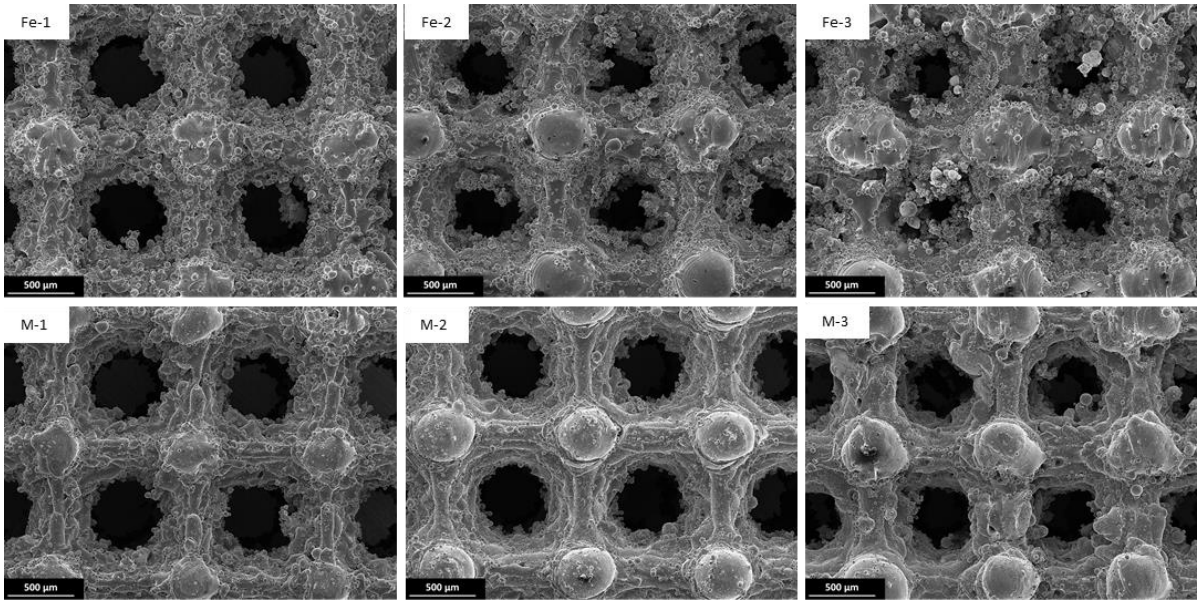

Figure 3 Surface morphologies of as built pure Fe and Fe-35Mn (M) scaffolds with lowest energy density (1 at 32 J/mm3), optimised energy density (Fe-2 at 72 J/mm3, M-2 at 62 J/mm3) and highest energy density (3 at 113 J/mm3). Build direction is out of plane.

Despite the morphological differences, concerning the surface roughness no significant difference was present between different processing conditions and the employed material type The overall mean of the average roughness (Ra) of the pure Fe struts was 14.2 ± 1.3 µm, while for the Fe-35Mn it was 13.5 ± 3.6 µm. In Figure 5 the surface roughness parameters for the two materials are shown. These values are comparable to the surface roughness of large components along the build direction [61].

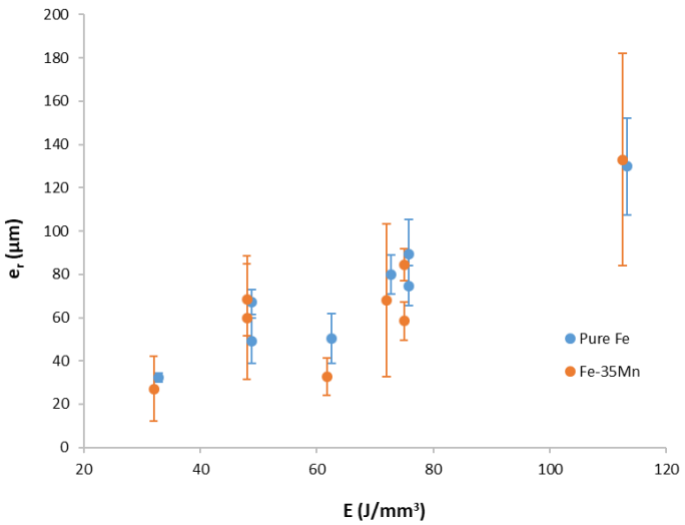

Figure 4 The effect of energy density on the dimensional error of scaffold struts. Error bars represent standard deviation. Note that energy densities of pure Fe are slightly shifted for better visual representation

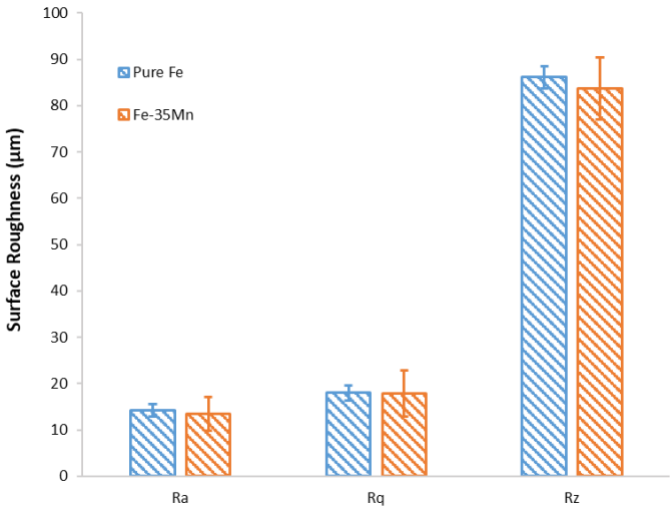

Figure 5 Surface roughness parameters of scaffold struts. Error bars represent standard deviation

3.2.2 Density and Hardness

Figure 6 shows that at the lowest energy density the scaffolds contain pores typical of partial fusing of the powder. Similarly, at the highest energy density the porosities are spherical, typical of gas entrapment [67]. While both types of porosities are present in the samples with moderate energy densities, the pure Fe scaffold has a lot more porosities caused by a lack of fusion.

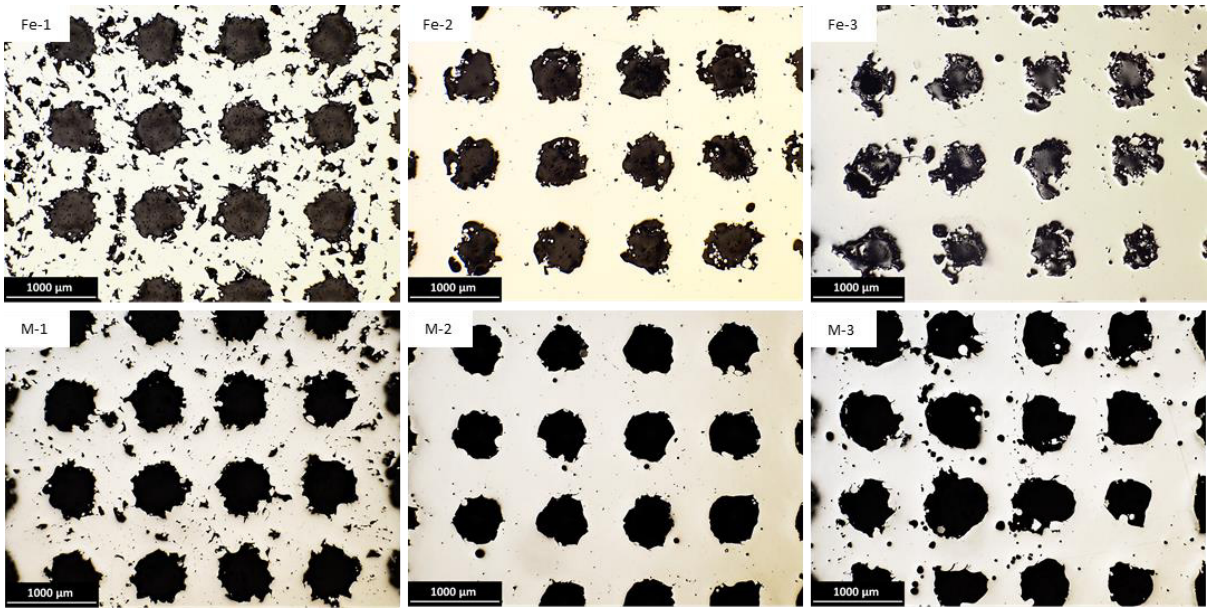

Figure 6 Cross-sectional micrographs of pure Fe and Fe-35Mn (M) scaffolds with lowest energy density (1 at 32 J/mm3), optimised energy density (Fe-2 at 72 J/mm3, M-2 at 62 J/mm3) and highest energy density (3 at 113 J/mm3). Build direction is out of plane.

From Figure 7-A an overall trend of increasing processed density with increasing energy density can be observed. This increase is expected and is associated with the increase in melt pool size with increasing energy density. It can also be seen that the processed density and dimensional error have a similar increasing trend with increasing energy density. This is because as the melt pool size increases, the closure of the designed porous structure and

the deviation from the designed density increases. Figure 7-B shows that the processing porosity of both metals increases with increasing energy density before reaching a minimum between 60-80 J/mm3, before increasing as the energy density becomes too high. The optimised conditions (shown in Table 3) resulted in low porosity struts ($\Phi < 0.6$ %) with a processed density of approximately 50% and a dimensional error of about 75 µm for pure Fe and 35 µm for Fe-35Mn.

Table 3 Optimised Parameters for pure Fe and Fe-35Mn scaffolds

Material	P (W)	t_{on} (µs)	$d_p = d_h$ (µm)	*Energy Density* (J/mm3)
Pure Fe	150	60	50	72
Fe-35Mn	125	50	45	62

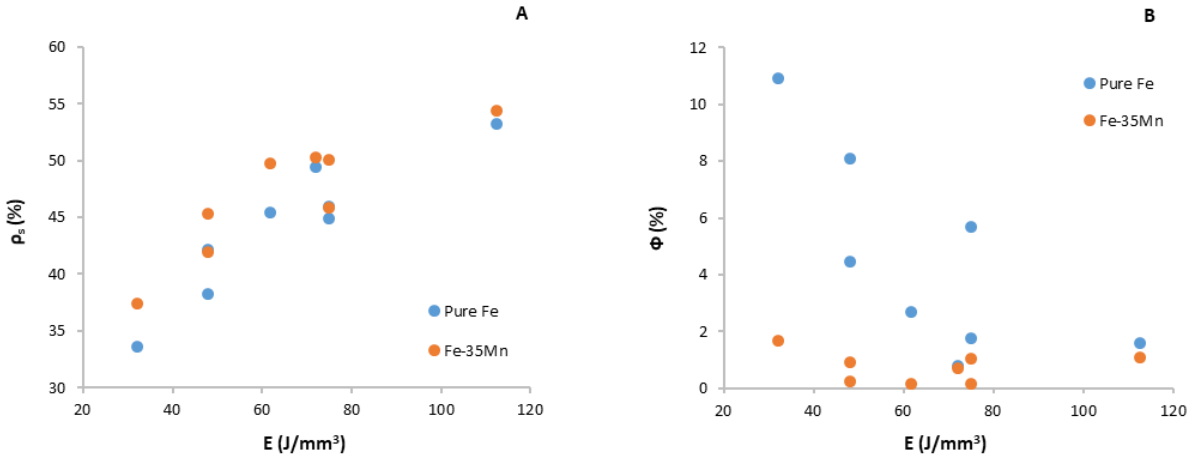

Figure 7 The effect of energy density on the processed density (A) and processing porosity (B). Error bars are omitted due to the difficulty in resolving them beyond the markers.

Table 4 provides a comparison between the microhardness values of the materials processed in this article with the "gold-standard" Fe-based biocompatible alloy AISI 316L and the other biodegradable metals Zn and Mg. The values are provided for different manufacturing processes, where available. The materials are also compared to the human bone. It can be seen that the SLM produced pure Fe and Fe-35Mn have characteristics comparable to the rolled mild steel, where as their hardness is superior to that of SLM produced pure Zn and pure Mg. According to the Hall-Petch relationship, the hardness of a polycrystalline metal will increase with decreasing grain size [68]. The α-ferrite in the pure Fe is softer than the austenite found in the Fe-35Mn [69] resulting in a lower overall 150 ± 6.5 Hv compared to 163 ± 4 Hv for the austenitic Fe-35Mn.

Table 4 Comparison of Vickers microhardness (HV) values of biodegradable metals and AISI 316L produced by different manufacturing methods compared to the human bone.

Human bone [70]	40-79

Material	SLM	Cast	Wrought
Pure Fe	150 ± 6.5	130 (Mild steel)	150 (Mild steel)
Fe-35Mn	163 ± 4.0	n/a	n/a
AISI 316L [52]	245 ± 6.0	175	220
Pure Zn [48]	45 ± 5.4	n/a	34±2
Pure Mg [71]	78 ± 8.2	30 ± 2	41 ± 2

3.2 Microstructure

The microstructure varied considerably between the pure Fe and Fe-35Mn as can be seen in Figure 8 and Figure 9. Despite the clear difference between the microstructure of the two materials, both materials did not vary greatly with changing processing parameters. As such, only the microstructure of the optimised structures is shown as it can be more clearly observed due to its lower processing porosity. The main defect type observed is related to lack of fusion, whereas use of high energy densities do not appear to be greatly vary grain size. The pure Fe has a relatively simple grain structure consisting of small α-ferrite grains. Small melt pools and high cooling rates typical of SLM [72] promote grain refinement resulting in finer grains when compared to traditional manufacturing methods [39]. It can also be seen that there is a difference in grain morphology and size between the planes relative to the build direction (BD), with an average grain size of 7.6 ± 1.2 μm with the BD out of plane (Figure 8 A) and 12.61 ± 2.9 μm with the BD in plane (Figure 8 B). It is well known that columnar grains grow preferentially in the direction opposite to the steepest thermal gradients, which in the case of SLM is towards the substrate, resulting in columnar grains in the plane of the build direction [73]. However, in the case of pure iron, while there are some directional grains, there appears to be no favourable growth direction, rather a mix of generally equiaxed grains with some taking on a more elongated orientation. This is not surprising given that the α-ferrite grains are a product of solid state transformation from the γ-austenite phase and thus are quite removed from the initial solidified structure ($L \rightarrow \delta \rightarrow \gamma \rightarrow \alpha$). It is therefore difficult to identify any residual features in the bulk pure Fe that shed light on the solidification process. Nevertheless, the directional heat extraction still occurs during the solid state transformations which may account for the slightly elongated grains in the build direction.

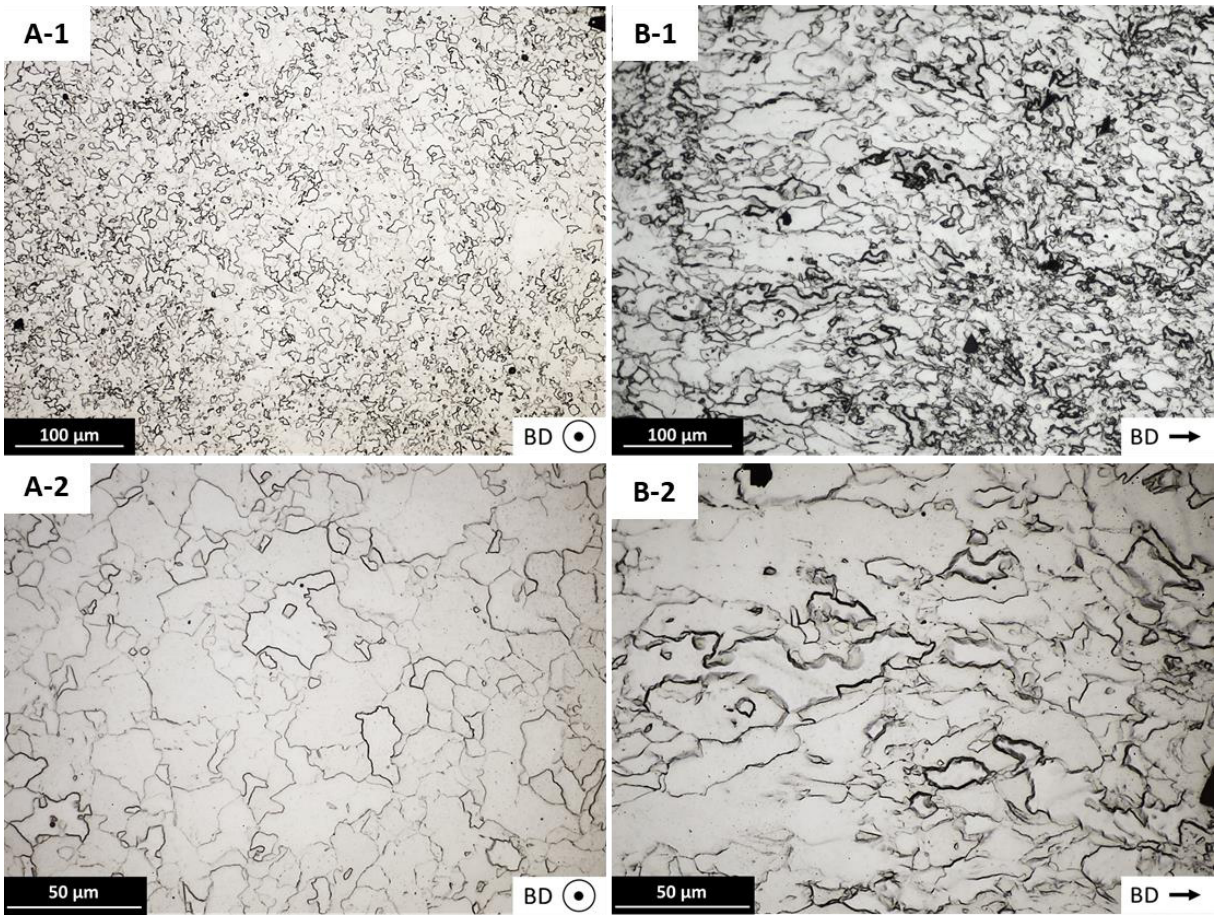

Figure 8 Pure Fe cross-sectional optical micrographs showing the microstructure at different magnifications with BD out of plane (A) and in plane (B)

In contrast, the addition of 35 wt% Mn stabilises the γ-austenite phase and preserves the solidified microstructure produced during SLM (L → γ). In general, each melt pool is comprised of several large columnar γ grains, which grow opposite to the direction of heat flow, and each γ-grain is comprised of a network of individual cells. Due to the alternating scan strategies which changes the directions of heat input and extraction, a complex array of direction changing γ grains result (for example see Figure 9 A-1). Epitaxial growth on favourably orientated grains also occurs occasionally creating long grains spanning across several melt pools (see Figure 9 B-2).

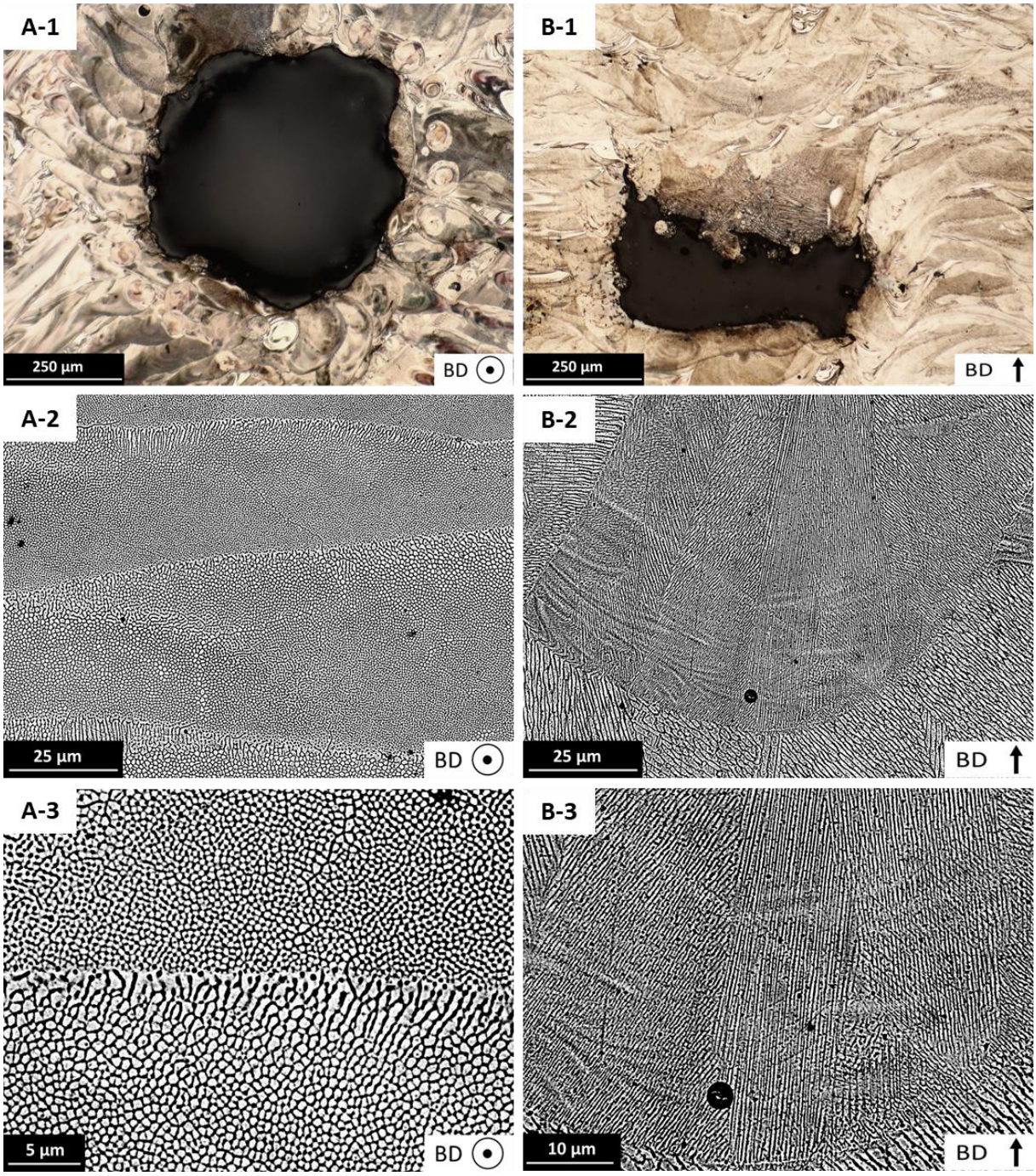

Figure 9 Fe-35Mn cross-sectional micrographs showing the melt pool outlines with BD out of plane (A-1) and BD in plane (B-1). SEM images showing the finer microstructural details with BD out of plane (A-2,3) and BD in plane (B-2,3). Please note a difference in scale bars between A and B to better show the features.

The cellular structure is apparent in the Fe-35Mn and not apparent in the pure Fe due to the segregation of Mn solute. At 35wt% Mn, according to the binary phase diagram [74], the partition coefficient k of Mn in Fe is approximately 0.73 which results in some Mn solute accumulation between the cells (the dark regions in Figure 9 A-3). The width of the individual cells varies throughout the melt pool (typically between 0.1-1 µm) and is related to differences in the local solidification rate. The predominance of the cellular solidification mode as opposed to dendritic is an indication of the high solidification rates encountered during SLM in addition to alloy specific factors that limits the development of constitutional supercooling. The development of constitutional

supercooling (ΔT_{cs}) has been extensively studied in Al [75], Mg [76] and Ti alloys [77] and the relative contribution of a solute to ΔT_{cs} can be assessed using the growth restriction factor, Q using phase diagram information given by Equation (5):

$$Q = m_L c_0(k\text{-}1) \qquad (5)$$

Where m_L is the liquidus gradient and c_0 is the solute concentration in wt%. In the present case for Mn solute, Q = 0.07 c_0 which is very low compared to effective solutes in other alloy systems [75], indicating that Mn solute will develop limited constitutional supercooling and likely accounts for the absence of a dendritic solidification mode. Even with 35wt% solute, $Q \approx 2.45$ °C and thus Mn solute in this alloy is expected to provide limited growth restriction and have a minor contribution refining the primary γ-grains during solidification. Therefore, although the primary solidified δ-grains are not observable in the pure Fe microstructure, it is reasonable to expect that their initial grain size and shape would be comparable to those clearly visible in Fe-35Mn unless the population of nucleant particles varied between each alloy.

Conclusion

This study investigated the influence of laser processing parameters on scaffolds of pure Fe and Fe-35Mn for biodegradable implant applications. Using an experimental design approach, laser processing parameters were successfully optimised to manufacture high quality scaffolds. The results can be summarised as follows:

- Scaffolds with a processing porosity less than 0.6 % were successfully manufactured for both pure Fe and Fe-35Mn. The lower melting temperature of the Fe-35Mn was advantageous for scaffolds and was thus easier to process than the pure Fe.
- Scaffold quality was determined by its resemblance to the original CAD model. This requires the investigation of designed pore size and porosity as a process defect together. Using this key indicator, moderate energy density levels (60-80 J/cm^3) are required to achieve high density thin struts.
- The surface roughness of the scaffolds were comparable to the bulk material in as-built state.
- The microhardness values of the pure Fe and the Fe-35Mn were found to be comparable to a mild steel and much greater than the pure Zn and pure Mg counterparts.
- Distinct microstructures were observed for the pure metal and the binary alloy, reflecting also the differences in the processability. The microstructure of pure Fe was characterized by mostly equiaxed α-ferrite grains with no evidence of the original solidification structure. The addition of 35wt% Mn stabilises the γ-austenite phase and reveals a solidified microstructure of columnar γ grains, each comprising of a network of individual cells.

Acknowledgements

DC, MJB and MSD acknowledge the support of the School of Mechanical and Mining Engineering, the Queensland Centre for Advanced Materials processing and Manufacturing and the Australian Research Council Research Hub for Advanced Manufacturing of Medical Devices (IH150100024). AGD, LC and BP acknowledge the support of European Union, Repubblica Italiana, Regione Lombardia and FESR for the project MADE4LO under the call "POR FESR 2014-2020 ASSE I - AZIONE I.1.B.1.3". MJB also acknowledges the support of the

Australian Research Council Discovery Program and is in receipt of Discover Early Career Researcher Award (DE160100260).

References

[1] A. Barone, U. Covani, Maxillary Alveolar Ridge Reconstruction With Nonvascularized Autogenous Block Bone: Clinical Results, Journal of Oral and Maxillofacial Surgery 65(10) (2007) 2039-2046.
[2] A.A. Jahangir, ;, R.M. Nunley, S. Mehta, A. Sharan, Bone graft substitutes in orthopaedic surgery, AAOS Now 2 (2008) 35-37.
[3] F. Chamieh, A.-M. Collignon, B.R. Coyac, J. Lesieur, S. Ribes, J. Sadoine, A. Llorens, A. Nicoletti, D. Letourneur, M.-L. Colombier, S.N. Nazhat, P. Bouchard, C. Chaussain, G.Y. Rochefort, Accelerated craniofacial bone regeneration through dense collagen gel scaffolds seeded with dental pulp stem cells, 6 (2016) 38814.
[4] J.A. Goulet, L.E. Senunas, G.L. DeSilva, M.L. Greenfield, Autogenous iliac crest bone graft. Complications and functional assessment, Clinical orthopaedics and related research (339) (1997) 76-81.
[5] J.S. Silber, D.G. Anderson, S.D. Daffner, B.T. Brislin, J.M. Leland, A.S. Hilibrand, A.R. Vaccaro, T.J. Albert, Donor site morbidity after anterior iliac crest bone harvest for single-level anterior cervical discectomy and fusion, Spine 28(2) (2003) 134-9.
[6] R.A. Kenley, K. Yim, J. Abrams, E. Ron, T. Turek, L.J. Marden, J.O. Hollinger, Biotechnology and Bone Graft Substitutes, Pharmaceutical Research 10(10) (1993) 1393-1401.
[7] D.W. Hutmacher, Scaffolds in tissue engineering bone and cartilage, Biomaterials 21(24) (2000) 2529-2543.
[8] M. Niinomi, Recent metallic materials for biomedical applications, Metallurgical and Materials Transactions A 33(3) (2002) 477.
[9] X. Liu, P.X. Ma, Polymeric scaffolds for bone tissue engineering, Annals of biomedical engineering 32(3) (2004) 477-86.
[10] A.R. Studart, U.T. Gonzenbach, E. Tervoort, L.J. Gauckler, Processing Routes to Macroporous Ceramics: A Review, Journal of the American Ceramic Society 89(6) (2006) 1771-1789.
[11] M. Navarro, A. Michiardi, O. Castaño, J.A. Planell, Biomaterials in orthopaedics, Journal of the Royal Society Interface 5(27) (2008) 1137-1158.
[12] L. Roseti, V. Parisi, M. Petretta, C. Cavallo, G. Desando, I. Bartolotti, B. Grigolo, Scaffolds for Bone Tissue Engineering: State of the art and new perspectives, Materials Science and Engineering: C 78 (2017) 1246-1262.
[13] S. Bose, M. Roy, A. Bandyopadhyay, Recent advances in bone tissue engineering scaffolds, Trends in Biotechnology 30(10) (2012) 546-554.
[14] D.F. Williams, On the mechanisms of biocompatibility, Biomaterials 29(20) (2008) 2941-2953.
[15] J.E. Davies, R. Matta, V.C. Mendes, P.S. Perri de Carvalho, Development, characterization and clinical use of a biodegradable composite scaffold for bone engineering in oro-maxillo-facial surgery, Organogenesis 6(3) (2010) 161-6.
[16] R.M. Meneghini, D.G. Lewallen, A.D. Hanssen, Use of porous tantalum metaphyseal cones for severe tibial bone loss during revision total knee replacement, The Journal of bone and joint surgery. American volume 90(1) (2008) 78-84.
[17] J.D. Bobyn, G.J. Stackpool, S.A. Hacking, M. Tanzer, J.J. Krygier, Characteristics of bone ingrowth and interface mechanics of a new porous tantalum biomaterial, The Journal of bone and joint surgery. British volume 81(5) (1999) 907-14.
[18] A. Curodeau, E. Sachs, S. Caldarise, Design and fabrication of cast orthopedic implants with freeform surface textures from 3-D printed ceramic shell, Journal of biomedical materials research 53(5) (2000) 525-35.
[19] F.A. Shah, O. Omar, F. Suska, A. Snis, A. Matic, L. Emanuelsson, B. Norlindh, J. Lausmaa, P. Thomsen, A. Palmquist, Long-term osseointegration of 3D printed CoCr constructs with an interconnected open-pore architecture prepared by electron beam melting, Acta Biomaterialia 36 (2016) 296-309.

[20] S. Van Bael, Y.C. Chai, S. Truscello, M. Moesen, G. Kerckhofs, H. Van Oosterwyck, J.P. Kruth, J. Schrooten, The effect of pore geometry on the in vitro biological behavior of human periosteum-derived cells seeded on selective laser-melted Ti6Al4V bone scaffolds, Acta Biomaterialia 8(7) (2012) 2824-2834.
[21] G.E. Ryan, A.S. Pandit, D.P. Apatsidis, Porous titanium scaffolds fabricated using a rapid prototyping and powder metallurgy technique, Biomaterials 29(27) (2008) 3625-3635.
[22] Y. Okazaki, E. Gotoh, Comparison of metal release from various metallic biomaterials in vitro, Biomaterials 26(1) (2005) 11-21.
[23] M. Geetha, A.K. Singh, R. Asokamani, A.K. Gogia, Ti based biomaterials, the ultimate choice for orthopaedic implants – A review, Progress in Materials Science 54(3) (2009) 397-425.
[24] Y.F. Zheng, X.N. Gu, F. Witte, Biodegradable metals, Materials Science and Engineering: R: Reports 77 (2014) 1-34.
[25] H. Li, Y. Zheng, L. Qin, Progress of biodegradable metals, Progress in Natural Science: Materials International 24(5) (2014) 414-422.
[26] M.G. Seelig, A study of magnesium wire as an absorbable suture and ligature material, Archives of Surgery 8(2) (1924) 669-680.
[27] M.P. Staiger, A.M. Pietak, J. Huadmai, G. Dias, Magnesium and its alloys as orthopedic biomaterials: A review, Biomaterials 27(9) (2006) 1728-1734.
[28] F. Witte, Reprint of: The history of biodegradable magnesium implants: A review, Acta Biomaterialia 23 (2015) S28-S40.
[29] P.K. Bowen, J. Drelich, J. Goldman, Zinc Exhibits Ideal Physiological Corrosion Behavior for Bioabsorbable Stents, Advanced Materials 25(18) (2013) 2577-2582.
[30] E. Mostaed, M. Sikora-Jasinska, A. Mostaed, S. Loffredo, A.G. Demir, B. Previtali, D. Mantovani, R. Beanland, M. Vedani, Novel Zn-based alloys for biodegradable stent applications: Design, development and in vitro degradation, Journal of the Mechanical Behavior of Biomedical Materials 60 (2016) 581-602.
[31] P.K. Bowen, E.R. Shearier, S. Zhao, R.J. Guillory, F. Zhao, J. Goldman, J.W. Drelich, Biodegradable Metals for Cardiovascular Stents: from Clinical Concerns to Recent Zn-Alloys, Advanced Healthcare Materials 5(10) (2016) 1121-1140.
[32] M. Peuster, P. Wohlsein, M. Brügmann, M. Ehlerding, K. Seidler, C. Fink, H. Brauer, A. Fischer, G. Hausdorf, A novel approach to temporary stenting: degradable cardiovascular stents produced from corrodible metal—results 6–18 months after implantation into New Zealand white rabbits, Heart 86(5) (2001) 563.
[33] M. Schinhammer, A.C. Hänzi, J.F. Löffler, P.J. Uggowitzer, Design strategy for biodegradable Fe-based alloys for medical applications, Acta Biomaterialia 6(5) (2010) 1705-1713.
[34] H. Hermawan, D. Dubé, D. Mantovani, Degradable metallic biomaterials: Design and development of Fe–Mn alloys for stents, Journal of Biomedical Materials Research Part A 93A(1) (2010) 1-11.
[35] H. Hermawan, D. Dube, D. Mantovani, Degradable metallic biomaterials: design and development of Fe-Mn alloys for stents, Journal of biomedical materials research. Part A 93(1) (2010) 1-11.
[36] B. Liu, Y.F. Zheng, Effects of alloying elements (Mn, Co, Al, W, Sn, B, C and S) on biodegradability and in vitro biocompatibility of pure iron, Acta Biomaterialia 7(3) (2011) 1407-1420.
[37] M. Moravej, F. Prima, M. Fiset, D. Mantovani, Electroformed iron as new biomaterial for degradable stents: Development process and structure–properties relationship, Acta Biomaterialia 6(5) (2010) 1726-1735.
[38] D. Hong, D.-T. Chou, O.I. Velikokhatnyi, A. Roy, B. Lee, I. Swink, I. Issaev, H.A. Kuhn, P.N. Kumta, Binder-jetting 3D printing and alloy development of new biodegradable Fe-Mn-Ca/Mg alloys, Acta Biomaterialia 45 (2016) 375-386.
[39] Y. Li, H. Jahr, K. Lietaert, P. Pavanram, A. Yilmaz, L.I. Fockaert, M.A. Leeflang, B. Pouran, Y. Gonzalez-Garcia, H. Weinans, J.M.C. Mol, J. Zhou, A.A. Zadpoor, Additively manufactured biodegradable porous iron, Acta Biomaterialia 77 (2018) 380-393.

[40] A. Fukuda, M. Takemoto, T. Saito, S. Fujibayashi, M. Neo, D.K. Pattanayak, T. Matsushita, K. Sasaki, N. Nishida, T. Kokubo, T. Nakamura, Osteoinduction of porous Ti implants with a channel structure fabricated by selective laser melting, Acta Biomaterialia 7(5) (2011) 2327-2336.
[41] V.K. Balla, S. Bodhak, S. Bose, A. Bandyopadhyay, Porous tantalum structures for bone implants: Fabrication, mechanical and in vitro biological properties, Acta Biomaterialia 6(8) (2010) 3349-3359.
[42] R. Wauthle, J. van der Stok, S. Amin Yavari, J. Van Humbeeck, J.-P. Kruth, A.A. Zadpoor, H. Weinans, M. Mulier, J. Schrooten, Additively manufactured porous tantalum implants, Acta Biomaterialia 14 (2015) 217-225.
[43] L. Hao, S. Dadbakhsh, O. Seaman, M. Felstead, Selective laser melting of a stainless steel and hydroxyapatite composite for load-bearing implant development, Journal of Materials Processing Technology 209(17) (2009) 5793-5801.
[44] C. Yan, L. Hao, A. Hussein, P. Young, D. Raymont, Advanced lightweight 316L stainless steel cellular lattice structures fabricated via selective laser melting, Materials & Design 55 (2014) 533-541.
[45] F. Witte, L. Jauer, W. Meiners, Z. Kronbach, K. Strohschein, T. Schmidt, Open-porous biodegradable magnesium scaffolds produced by selective laser melting for individualized bone replacement, Frontiers in Bioengineering and Biotechnology.
[46] Y. Li, J. Zhou, P. Pavanram, M.A. Leeflang, L.I. Fockaert, B. Pouran, N. Tümer, K.U. Schröder, J.M.C. Mol, H. Weinans, H. Jahr, A.A. Zadpoor, Additively manufactured biodegradable porous magnesium, Acta Biomaterialia 67 (2018) 378-392.
[47] M. Gieseke, C. Noelke, S. Kaierle, V. Wesling, H. Haferkamp, Selective Laser Melting of Magnesium and Magnesium Alloys, in: N. Hort, S.N. Mathaudhu, N.R. Neelameggham, M. Alderman (Eds.), Magnesium Technology 2013, Springer International Publishing, Cham, 2016, pp. 65-68.
[48] C. Liu, M. Zhang, C. Chen, Effect of laser processing parameters on porosity, microstructure and mechanical properties of porous Mg-Ca alloys produced by laser additive manufacturing, Materials Science and Engineering: A 703 (2017) 359-371.
[49] Lucas Jauer, Wilhelm Meiners, Simon Vervoort, Christoph Gayer, Naemi A. Zumdick, Daniela Zander, Selective Laser Melting of Magnesium Alloys, World PM 2016, 2016.
[50] N.A. Zumdick, L. Jauer, L.C. Kersting, T.N. Kutz, J.H. Schleifenbaum, D. Zander, Additive manufactured WE43 magnesium: A comparative study of the microstructure and mechanical properties with those of powder extruded and as-cast WE43, Materials Characterization 147 (2019) 384-397.
[51] A. International, A.I.H. Committee, A.I.A.P.D. Committee, Metals Handbook: Properties and selection, Asm International1990.
[52] A.G. Demir, L. Monguzzi, B. Previtali, Selective laser melting of pure Zn with high density for biodegradable implant manufacturing, Additive Manufacturing 15 (2017) 20-28.
[53] M. Marco, D. Ali Gökhan, M. Ehsan, V. Maurizio, P. Barbara, Processability of pure Zn and pure Fe by SLM for biodegradable metallic implant manufacturing, Rapid Prototyping Journal 23(3) (2017) 514-523.
[54] P. Wen, L. Jauer, M. Voshage, Y. Chen, R. Poprawe, J.H. Schleifenbaum, Densification behavior of pure Zn metal parts produced by selective laser melting for manufacturing biodegradable implants, Journal of Materials Processing Technology 258 (2018) 128-137.
[55] P. Wen, M. Voshage, L. Jauer, Y. Chen, Y. Qin, R. Poprawe, J.H. Schleifenbaum, Laser additive manufacturing of Zn metal parts for biodegradable applications: Processing, formation quality and mechanical properties, Materials & Design 155 (2018) 36-45.
[56] P. Wen, Y. Qin, Y. Chen, M. Voshage, L. Jauer, R. Poprawe, J. Henrich Schleifenbaum, Laser additive manufacturing of Zn porous scaffolds: shielding gas flow, surface quality and densification, Journal of Materials Science & Technology (2018).
[57] H. Fayazfar, M. Salarian, A. Rogalsky, D. Sarker, P. Russo, V. Paserin, E. Toyserkani, A critical review of powder-based additive manufacturing of ferrous alloys: Process parameters, microstructure and mechanical properties, Materials & Design 144 (2018) 98-128.

[58] M. Montani, A.G. Demir, E. Mostaed, M. Vedani, B. Previtali, Processability of pure Zn and pure Fe by SLM for biodegradable metallic implant manufacturing, Rapid Prototyping Journal 23(3) (2017) 514-523.
[59] B. Song, S. Dong, S. Deng, H. Liao, C. Coddet, Microstructure and tensile properties of iron parts fabricated by selective laser melting, Optics & Laser Technology 56 (2014) 451-460.
[60] T. Niendorf, F. Brenne, P. Hoyer, D. Schwarze, M. Schaper, R. Grothe, M. Wiesener, G. Grundmeier, H.J. Maier, Processing of New Materials by Additive Manufacturing: Iron-Based Alloys Containing Silver for Biomedical Applications, Metallurgical and Materials Transactions A 46(7) (2015) 2829-2833.
[61] A.G. Demir, B. Previtali, Additive manufacturing of cardiovascular CoCr stents by selective laser melting, Materials & Design 119 (2017) 338-350.
[62] A. Gökhan Demir, C. De Giorgi, B. Previtali, Design and Implementation of a Multisensor Coaxial Monitoring System With Correction Strategies for Selective Laser Melting of a Maraging Steel, Journal of Manufacturing Science and Engineering 140(4) (2018) 041003-041003-14.
[63] A.B. Spierings, G. Levy, Comparison of Density of Stainless Steel316 L Parts Produced With Selective Laser Melting Using Different Powder Grades, International Solid Freeform Fabrication Symposium (SFF), Austin,TX, 2009, pp. 342-353.
[64] S. Rajagopalan, R.A. Robb, Schwarz meets Schwann: Design and fabrication of biomorphic and durataxic tissue engineering scaffolds, Medical Image Analysis 10(5) (2006) 693-712.
[65] J. Shin, S. Kim, D. Jeong, H.G. Lee, D. Lee, J.Y. Lim, J. Kim, Finite Element Analysis of Schwarz P Surface Pore Geometries for Tissue-Engineered Scaffolds, Mathematical Problems in Engineering 2012 (2012) 13.
[66] ASTM International, Standard Test Methods for Determining Average Grain Size, ASTM International,, PA, United States, 2014.
[67] N.T. Aboulkhair, N.M. Everitt, I. Ashcroft, C. Tuck, Reducing porosity in AlSi10Mg parts processed by selective laser melting, Additive Manufacturing 1-4 (2014) 77-86.
[68] N. Hansen, Hall–Petch relation and boundary strengthening, Scripta Materialia 51(8) (2004) 801-806.
[69] W.D. Callister, D.G. Rethwisch, Materials science and engineering, Ninth edition, SI version.. ed., Singapore : John Wiley & Sons Asia Pte Ltd2015.
[70] H. Chung Man, C. Chung Ng, M. Savalani, Fabrication of magnesium using selective laser melting technique, Rapid Prototyping Journal 17(6) (2011) 479-490.
[71] E. Mostaed, M. Vedani, M. Hashempour, M. Bestetti, Influence of ECAP process on mechanical and corrosion properties of pure Mg and ZK60 magnesium alloy for biodegradable stent applications, Biomatter 4(1) (2014) e28283.
[72] L.-E. Loh, C.-K. Chua, W.-Y. Yeong, J. Song, M. Mapar, S.-L. Sing, Z.-H. Liu, D.-Q. Zhang, Numerical investigation and an effective modelling on the Selective Laser Melting (SLM) process with aluminium alloy 6061, International Journal of Heat and Mass Transfer 80 (2015) 288-300.
[73] L. Thijs, F. Verhaeghe, T. Craeghs, J.V. Humbeeck, J.-P. Kruth, A study of the microstructural evolution during selective laser melting of Ti–6Al–4V, Acta Materialia 58(9) (2010) 3303-3312.
[74] V.T. Witusiewicz, F. Sommer, E.J. Mittemeijer, Reevaluation of the Fe-Mn phase diagram, Journal of Phase Equilibria and Diffusion 25(4) (2004) 346-354.
[75] M.A. Easton, D.H. StJohn, A model of grain refinement incorporating alloy constitution and potency of heterogeneous nucleant particles, Acta Materialia 49(10) (2001) 1867-1878.
[76] D.H. StJohn, M. Qian, M.A. Easton, P. Cao, Z. Hildebrand, Grain refinement of magnesium alloys, Metallurgical and Materials Transactions A 36(7) (2005) 1669-1679.
[77] M. Bermingham, S. McDonald, M. Dargusch, D. StJohn, Grain-refinement mechanisms in titanium alloys, Journal of Materials Research 23(1) (2008) 97-104.